JACS
JOURNAL OF THE AMERICAN CHEMICAL SOCIETY
pubs.acs.org/JACS
Article

Liquid-Phase van der Waals Epitaxy of a Few-Layer and Unit-Cell Thick Ruddlesden–Popper Halide Perovskite

Lifu Zhang, Jie Jiang, Yang Hu, Zonghuan Lu, Xixing Wen, Saloni Pendse, Ru Jia, Gwo-Ching Wang, Toh-Ming Lu, and Jian Shi*

Cite This: J. Am. Chem. Soc. 2022, 144, 17588–17596
Read Online
ACCESS | Metrics & More | Article Recommendations | Supporting Information

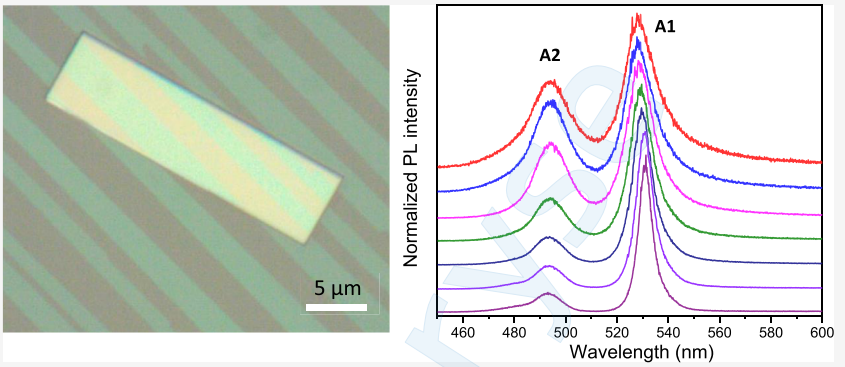

ABSTRACT: 2D Ruddlesden–Popper (RP) halide perovskites with natural multiple quantum well structures are an ideal platform to integrate into vertical heterostructures, which may introduce plentiful intriguing optoelectronic properties that are not accessible in a single bulk crystal. Here, we report liquid-phase van der Waals epitaxy of a 2D RP hybrid perovskite $(4,4\text{-DFPD})_2PbI_4$ (4,4-DFPD is 4,4-difluoropiperidinium) on muscovite mica and fabricate a series of perovskite–perovskite vertical heterostructures by integrating it with a second 2D RP perovskite R-NPB [NPB = 1-(1-naphthyl)ethylammonium lead bromide] sheets. The grown $(4,4\text{-DFPD})_2PbI_4$ nanobelt array can be multiple layers to unit-cell thin and are crystallographically aligned on the mica substrate. An interlayer photo emission in this R-NPB/$(4,4\text{-DFPD})_2PbI_4$ heterostructure with a lifetime of about 25 ns at 120 K has been revealed. Our demonstration of epitaxial $(4,4\text{-DFPD})_2PbI_4$ array grown on mica *via* liquid-phase van der Waals epitaxy provides a paradigm to prepare orderly distributed 2D RP hybrid perovskites for further integration into multiple heterostructures. The discovery of a new interlayer emission in the R-NPB/$(4,4\text{-DFPD})_2PbI_4$ heterostructure enriches the basic understanding of interlayer charge transition in halide perovskite systems.

INTRODUCTION

Two-dimensional van der Waals halide perovskites are a new class of emerging semiconductors whose flexibility of chemical composition,[1−3] enhanced stability in ambient conditions due to the hydrophobic organic layer,[4,5] multifunctionality,[6−9] and tunable optoelectronic properties[10−12] make them promising candidates for technologically relevant optoelectronics.[13−15] 2D Ruddlesden–Popper (RP) halide perovskites have a natural multiple quantum well structure where the stacked inorganic layers serve as the potential "well" and the interlayer organic cation chains serve as the potential "wall."[16−18] The inherent weak van der Waals interaction between the neighboring organic cation layers makes 2D RP perovskites an ideal platform to integrate with other layered materials to form heterostructures that can be harnessed for the design of intriguing optoelectronic functionalities which are not accessible in a single bulk crystal. Due to the low dielectric constant of the interlayer organic cations, their excitons residing in the wells with enhanced Coulomb interactions usually have a large binding energy,[19] allowing the design of perovskite excitonic devices. Inspired by the discoveries of many interesting interlayer excitonic phenomena in other van der Waals heterostructures such as 2D chalcogenides,[20−25] 2D RP halide perovskite heterostructures could also be exploited for exploring interesting excitonic physics.

To fabricate heterostructures utilizing 2D RP halide perovskites, the synthesis of RP halide perovskites with desired dimensionality and crystallographic orientation is highly in demand. Direct chemical synthesis of 2D RP perovskite–

Received: July 5, 2022
Published: September 13, 2022

https://doi.org/10.1021/jacs.2c07069
J. Am. Chem. Soc. 2022, 144, 17588–17596

perovskite heterostructures in solution has been reported,[26−30] but this method lacks control on the registration of the final structures (*i.e.*, not epitaxial). Moreover, the direct solution growth method is limited to adjusting the number of inorganic octahedra building blocks per van der Waals layer of neighboring perovskite phases. Recently, Pan *et al.*[3] reported a controllable growth of various 2D RP perovskites at the liquid−air interface and demonstrated a facile mechanical transfer method to fabricate arbitrary vertical heterostructures. However, these nanosheets are randomly distributed after growth, limiting the fabrication precision for heterostructures. Here, we propose a liquid-phase van der Waals epitaxial growth of 2D RP perovskite on layered substrates (muscovite mica), as shown in Figure 1. Unlike the randomly distributed sheets at the liquid−air interface, the grown RP perovskites on the substrate are expected to be well aligned with each other due to epitaxy.

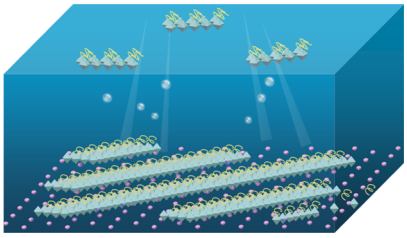

Figure 1. Schematic of liquid-phase van der Waals epitaxy of 2D RP halide perovskites on mica. For clarity, the mica substrate has been simplified with only the top potassium layer to show the pseudohexagonal symmetry, and only one layer of octahedron and organic functional group has been sketched to represent 2D RP perovskites.

In this work, we have successfully achieved the liquid-phase van der Waals epitaxial growth of a 2D RP perovskite (4,4-DFPD)$_2$PbI$_4$ (4,4-DFPD is 4,4-difluoropiperidinium) on muscovite mica *via* a modified dissolution−recrystallization process.[31] By stacking another 2D RP perovskite R-NPB [NPB = 1-(1-naphthyl)ethylammonium lead bromide] onto the synthesized horizontally aligned (4,4-DFPD)$_2$PbI$_4$ belt arrays, we found a type I interlayer emission in this R-NPB/(4,4-DFPD)$_2$PbI$_4$ vertical heterostructure. Our demonstration of epitaxial (4,4-DFPD)$_2$PbI$_4$ grown on mica *via* liquid-phase van der Waals epitaxy provides a paradigm to prepare orderly distributed 2D RP hybrid perovskites for further integration into heterostructures.

RESULTS

Figure 2a is an atomic model of (4,4-DFPD)$_2$PbI$_4$ we aim to grow. The typical growth condition is as follows. First, several droplets of HI aqueous solution with saturated (4,4-DFPD)$_2$PbI$_4$ were dropped on the fresh and clean surface of a flat mica substrate. Second, the mica substrate covered with a flat liquid layer was then placed in a chemical hood at room temperature. Third, water in the solution evaporates steadily, favoring the nucleation and growth of (4,4-DFPD)$_2$PbI$_4$. More details are presented in the Methods section. The as-grown crystals have been confirmed to be (4,4-DFPD)$_2$PbI$_4$ by X-ray diffraction (XRD) (Figure S1). Figure 2b shows that the (4,4-DFPD)$_2$PbI$_4$ belts grown on mica are aligned in one direction. The surface height profile of these belts was further determined by atomic force microscopy (AFM), which is around 22 nm (9 unit cells), as shown in Figure 2c. The width of (4,4-DFPD)$_2$PbI$_4$ belt and the interval between neighboring belts can be adjusted by controlling the volume of the solution layer. For a thinner liquid layer, thinner and narrower belts can be formed, as shown in Figure 2d,e. The thickness of (4,4-DFPD)$_2$PbI$_4$ belts in Figure 2d is around 5 nm (Figure S2a), corresponding to 2 unit cells. (4,4-DFPD)$_2$PbI$_4$ belts with unit-cell thickness can also be found after growth (Figure 2f). From optical microscopy images, it can be seen that most belts are aligned in one direction, though occasionally, some other orientations can be observed (*e.g.* Figure S2b,c).

Electron backscatter diffraction (EBSD) analysis was further performed to reveal the epitaxial relationship between the horizontally aligned (4,4-DFPD)$_2$PbI$_4$ belts and the mica substrate (Figures 2g−i and S3). Figure 2g displays an EBSD pattern quality map (Kikuchi band) of a thick (4,4-DFPD)$_2$PbI$_4$ belt. The obvious Kikuchi bands were indexed (see details in Figure S3a), and they are all from the (4,4-DFPD)$_2$PbI$_4$ crystal. From the inverse pole figure (Figure 2h), we know the surface normal direction is [001], while the in-plane orientations are [010]||X and [100]||Y. Note that the (010)/(100) pole is not strictly aligned to the X/Y direction (∼5−10° shift), which is due to imperfect sample mounting and alignments on the EBSD sample holder. No signals from the mica substrate were detected because this (4,4-DFPD)$_2$PbI$_4$ belt is thick [thinner (4,4-DFPD)$_2$PbI$_4$ belts can be partially damaged by focused electron beam during measurement]. We then collected EBSD signals of mica near this (4,4-DFPD)$_2$PbI$_4$ belt under the same coordinate system (Figure S3b,c). By indexing the Kikuchi bands of the mica substrate with the misalignment and possible substrate distortion considered, its surface normal direction can be identified to be [001] and the in-plane orientations are [310]||X ([310] is the normal direction of the (110) crystal plane) and [$\bar{1}$10]||Y {[$\bar{1}$10] is the normal direction of ($\bar{1}$30) crystal plane}, as indicated in the inverse pole figure of Figure 2i. The out-of-plane orientation of both (4,4-DFPD)$_2$PbI$_4$ and mica was further confirmed by XRD (Figure S4).

Based on these analyses, the epitaxial relationship between horizontally aligned (4,4-DFPD)$_2$PbI$_4$ belts and the mica substrate can be determined. Figure 2j is a schematic showing the crystallographic orientation of aligned (4,4-DFPD)$_2$PbI$_4$ belts grown on the mica substrate. The mica lattice is pseudohexagonal,[32] while the perovskite in-plane lattice, on the other hand, has a 2-fold symmetry. (4,4-DFPD)$_2$PbI$_4$ belts are crystallized with (001) as the top facet and (100) and (010) as the side walls. The epitaxial relationship is (4,4-DFPD)$_2$PbI$_4$[001]||mica [001] and (4,4-DFPD)$_2$PbI$_4$[010]||mica [310]. There is an offset angle $\gamma \sim 30°$ between the mica [100] and the 2D perovskite [010]. To better understand the microscopic mechanism for such an epitaxy, we calculated the optimized lattice registration between (4,4-DFPD)$_2$PbI$_4$ and the mica substrate *via* geometrical superlattice area mismatching (GSAM) method (Figure S5).[33−36] The details of this GSAM method are described in the Methods section. The optimized rotation angles based on GSAM are around 0, 30, 60, and 90°. Our experimental observation is consistent with the calculated results. We have also used substrates such as r-sapphire ($1\bar{1}02$) and silicon (100) to grow (4,4-DFPD)$_2$PbI$_4$ (Figure S6). (4,4-DFPD)$_2$PbI$_4$ crystals grown on both r-sapphire and silicon are still beltlike. However, they are randomly distributed with different orientations. Compared to mica, we have found that there are less crystals on either

https://doi.org/10.1021/jacs.2c07069
J. Am. Chem. Soc. 2022, 144, 17588−17596

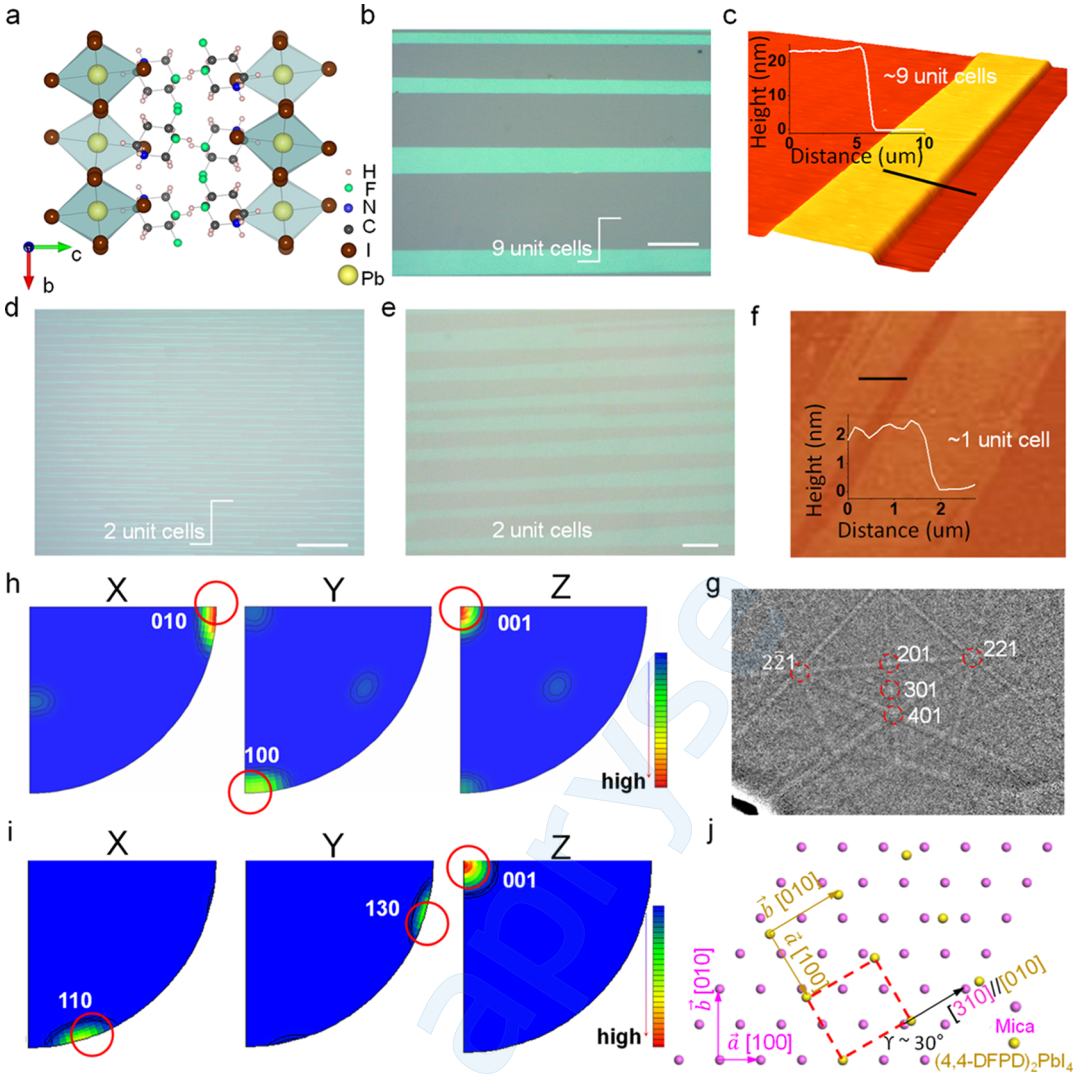

Figure 2. Morphology and structural analyses of (4,4-DFPD)$_2$PbI$_4$ belt arrays on mica. (a) Atomic model of (4,4-DFPD)$_2$PbI$_4$. (b) Optical image of a (4,4-DFPD)$_2$PbI$_4$ belt array grown on mica with parallel configuration. (c) AFM image of the belt array in (b). Inset is the height profile extracted along the black solid line with its thickness labeled. (d,e) Optical image of thinner and narrower (4,4-DFPD)$_2$PbI$_4$ belts under low magnification (d) and high magnification (e). (f) Monolayer (4,4-DFPD)$_2$PbI$_4$ grown on mica. Inset is the height profile extracted along the white solid line with its thickness labeled. (g) EBSD pattern quality map on a thick (4,4-DFPD)$_2$PbI$_4$ belt (>100 nm) with Kikuchi bands presented. (h) Inverse pole figures transformed from (g). Note that the (010) pole is not strictly aligned to the *X* direction (~5−10° shift), which is due to imperfect sample mounting and alignments on the EBSD sample holder, the same as the (100) pole in the *Y* direction. (i) Inverse pole figures of the mica substrate near the thick (4,4-DFPD)$_2$PbI$_4$ belt in (g). (j) Reconstructed lattice map representing the epitaxial relationship of horizontally aligned (4,4-DFPD)$_2$PbI$_4$ belts grown on the mica substrate. The lattice points of mica and (4,4-DFPD)$_2$PbI$_4$ are shown as purple and light-yellow dots, respectively. Main crystallographic directions of mica/(4,4-DFPD)$_2$PbI$_4$ perovskite are shown by purple/light-yellow arrows. The combined superlattice is shown by red dashed lines. Scale bars: 20 μm in (b), 50 μm in (d), and 5 μm in (e).

substrate of Si or r-plane sapphire. This is likely due to the poor wettability between (4,4-DFPD)$_2$PbI$_4$ and these two substrates.

Figure 3a,b shows the temperature-dependent photoluminescence (PL) study on (4,4-DFPD)$_2$PbI$_4$ belts with different thicknesses. For a thick (4,4-DFPD)$_2$PbI$_4$ belt (~0.87 μm, inset of Figures 3a and S7a), the peak energy changes from ~2.34 to ~2.35 eV as the temperature increases from 120 to 240 K. This blueshift is consistent with most bulk halide perovskites,[37,38] and it involves the ionic nature of Pb−I bonds which carry a net positive deformation potential[39,40] (more information can be found in Figure S8). For very thin (4,4-DFPD)$_2$PbI$_4$ belts (4 unit cells, inset of Figures 3b and S7b), the peak energy changes from ~2.37 to ~2.38 eV when the temperature increases from 120 to 240 K. It has a similar trend compared with the thick one as the temperature changes. However, we can find that there is ~0.03 eV offset for the PL peak of these two samples at the same temperature. The thickness-dependent PL shift for halide perovskite has been observed and studied in several previous works but with multiple explanations.[41−47] For example, Dou *et al.*[41] and Liu *et al.*[42] have reported that the blueshift of PL emission for the ultrathin perovskite sheets is related to the structural relaxation of the in-plane crystal lattice; Li *et al.*[43] suggest that the surface effect with the decreasing of the thickness plays an important role in this blueshift of PL emission. It is also likely due to quantum confinement effect.[46,47] We have also collected PL spectrum of unit-cell thick (4,4-DFPD)$_2$PbI$_4$ at a low

https://doi.org/10.1021/jacs.2c07069
J. Am. Chem. Soc. 2022, 144, 17588−17596

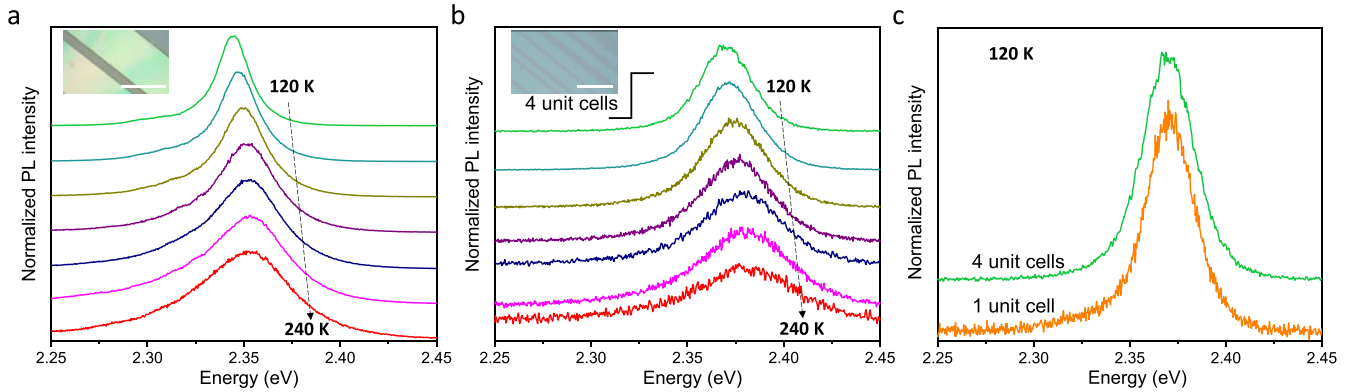

Figure 3. PL study of $(4,4\text{-DFPD})_2PbI_4$ belts on mica. (a) Temperature-dependent PL spectra of a thick $(4,4\text{-DFPD})_2PbI_4$ belt grown on mica. The temperature range is from 120 to 240 K with a step of 20 K per measurement. A blueshift of ∼0.01 eV of the main PL peak with increasing temperature is observed. Inset is an optical image of the thick $(4,4\text{-DFPD})_2PbI_4$ belt (∼0.87 μm from AFM image). (b) Temperature-dependent PL spectra of very thin $(4,4\text{-DFPD})_2PbI_4$ belts grown on mica. The temperature range is the same as that in (a). There is also a blueshift of ∼0.01 eV of the main PL peak with increasing temperature. Inset is an optical image of the measured thin $(4,4\text{-DFPD})_2PbI_4$ belts (4 unit cells from AFM image). (c) PL spectra of $(4,4\text{-DFPD})_2PbI_4$ with thicknesses of one unit cell and 4 unit cells grown on mica. The temperature is 120 K. Scale bars: 50 μm in (a) and 10 μm in (b).

temperature (120 K, Figure 3c). It shows that there is no obvious difference for the peak position compared with that of $(4,4\text{-DFPD})_2PbI_4$ belts with a thickness of 4 unit cells at the same temperature. Temperature-dependent PL study on single unit-cell thick crystal shows that the unit-cell thick film is easily damaged by the laser excitation (see Figure S9), calling further efforts to develop effective approaches to stabilize the film for reliable PL tests.

The $(4,4\text{-DFPD})_2PbI_4$ belts grown on mica *via* van der Waals epitaxy can be exfoliated from the mica substrate with the help of a polydimethylsiloxane soft stamp. Figure 4a displays a crossed array of $(4,4\text{-DFPD})_2PbI_4$ belts by stacking a horizontally aligned $(4,4\text{-DFPD})_2PbI_4$ array onto another horizontally aligned $(4,4\text{-DFPD})_2PbI_4$ array with an offset angle of ∼90°. This microcrossed array fabricated with 2D RP perovskites creates many homojunctions demonstrating a possible approach to fabricating twisted halide perovskites.

The mica substrate provides a solid base for the naturally grown $(4,4\text{-DFPD})_2PbI_4$ belts, which is helpful for them to be further processed into heterostructures in addition to the homostructures. A plethora of van der Waals heterostructures can be designed by covering these $(4,4\text{-DFPD})_2PbI_4$ belts with other different layered materials [*e.g.*, heterostructure of $(4,4\text{-DFPD})_2PbI_4/CsBiNb_2O_7$ as shown in Figure 4b,c]. The formed heterostructures are aligned with each other, and the twist angle between the top layer and bottom layer of a heterostructure can also be arbitrarily adjusted. Here, we mainly focus on a vertical heterostructure utilizing the grown $(4,4\text{-DFPD})_2PbI_4$ and another 2D RP halide perovskite R-NPB. R-NPB is a right-handed chiral 2D perovskite[48] with anionic $[PbBr_4]^{2-}$ layers of corner-sharing $PbBr_6$ octahedra separated by bilayers of NEA^+ cations [NEA = 1-(1-naphthyl)ethylamine]. It is synthesized *via* a solution method,[48] and its structure has been confirmed by XRD (Figure S10). Thin and flat R-NPB sheets are obtained by mechanically exfoliating a bulk R-NPB crystal with thermal release tape (more information can be found in Figure S11) and are then directly transferred onto the $(4,4\text{-DFPD})_2PbI_4$ belt array on the mica substrate. The atomic structure of an R-NPB/$(4,4\text{-DFPD})_2PbI_4$ vertical heterostructure is sketched in Figure 4d. According to ref 48, the band gap of R-NPB is about 3.1 eV. It emits white PL through the phonon-assisted emission process (*i.e.*, self-trapped excitons). Figure 4e is a schematic of band alignments for this heterostructure. The band gap of $(4,4\text{-DFPD})_2PbI_4$ is about 2.34 eV (corresponding to 530 nm) based on the temperature-dependent PL measurements in Figure 3a. The offset parameter $\Delta E_C/\Delta E_V$ for these two materials approximates to 1/4 based on the results observed in other iodine-based and bromine-based halide perovskites.[49] Thus, we can calculate ΔE_C to be 0.19 eV and ΔE_V to be 0.57 eV.

Based on this estimation, there are two possible interlayer emissions.[50−52] One is around 2.53 eV (490 nm) and the other is around 2.91 eV (426 nm), as represented by a cyan arrow and a dark blue arrow, respectively, in Figure 4e. Figure 4f shows the measured temperature-dependent PL spectra of an R-NPB/$(4,4\text{-DFPD})_2PbI_4$ heterostructure. An extra PL line labeled as A2 at around 494 nm (at 120 K) is indeed present, which is very close to our estimation of one proposed interlayer emission around 490 nm. Another proposed emission of 426 nm is not identified due to the detection limit of our CCD system. PL spectrum of pure R-NPB is also collected (the black dashed line in Figure 4f and the pink curve in Figure S12). As we can see, it is a broad spectrum of weak white light emission at 250 K, and there is no significant PL peak at around 490 nm. Similar PL results of R-NPB for other temperatures can be found in Figure S12. The new emission of A2 for the R-NPB/$(4,4\text{-DFPD})_2PbI_4$ heterostructure at different temperatures can be attributed to the interlayer exciton of this heterostructure. The intensity of the interlayer emission A2 increases as the temperature decreases from 240 to 120 K. This is common for interlayer excitons of many other different material systems such as incommensurate MoS_2/WSe_2 heterostructure and iso-$(C_4H_9NH_3)_2PbI_4/WSe_2$ heterostructure.[53,54] There is a similar trend for the intensity of the emission A1 from $(4,4\text{-DFPD})_2PbI_4$ as the temperature decreases, which may be related to the decrease in the rate of nonradiative thermal recombination with decreased thermal fluctuations.[55]

For the peak position, a blueshift occurs for A1 emission when the temperature increases from 120 to 240 K, which is consistent with the PL spectra results in Figure 3a. However,

https://doi.org/10.1021/jacs.2c07069
J. Am. Chem. Soc. 2022, 144, 17588−17596

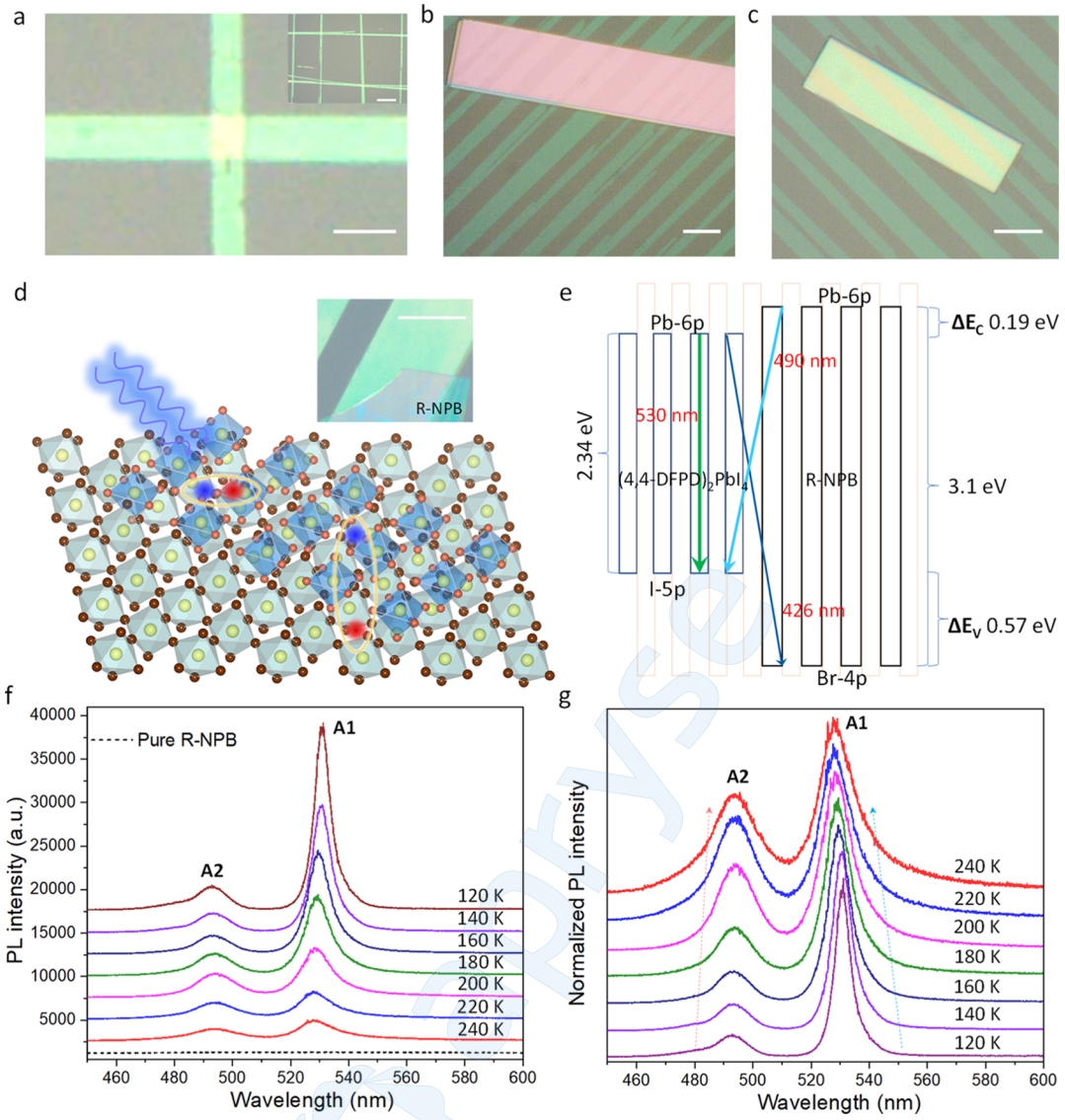

Figure 4. Design and PL characterization of $(4,4\text{-DFPD})_2PbI_4$-based homo/heterostructures. (a) Artificial crossed array of $(4,4\text{-DFPD})_2PbI_4$ belts with an intersectional angle of ~90°. Inset is a zoom-out image. (b,c) Optical image of a $(4,4\text{-DFPD})_2PbI_4$ belt array grown on mica with part of it covered by other different layered materials under different twist angles. (d) Schematic of the R-NPB/$(4,4\text{-DFPD})_2PbI_4$ vertical heterostructure. The top layer is R-NPB, while the bottom layer is $(4,4\text{-DFPD})_2PbI_4$. Inset is an optical image of a fabricated R-NPB/$(4,4\text{-DFPD})_2PbI_4$ heterostructure [the green belt is $(4,4\text{-DFPD})_2PbI_4$]. (e) Proposed band alignment for the R-NPB/$(4,4\text{-DFPD})_2PbI_4$ vertical heterostructure. (f) Temperature-dependent PL spectra of the R-NPB/$(4,4\text{-DFPD})_2PbI_4$ heterostructure. The temperature range is from 120 to 240 K with a step increment of 20 K. All signals are collected under an excitation fluence of 0.35 $\mu J/cm^2$ and an integral time of 10 s. The black dashed curve represents the PL spectrum of pure R-NPB at 250 K. (g) Normalized temperature-dependent PL spectra of this R-NPB/$(4,4\text{-DFPD})_2PbI_4$ heterostructure. The cyan dashed arrow indicates a blueshift of A1 emission, while the orange dashed arrow indicates a redshift of A2 emission as the temperature increases. Scale bars: 10 μm in (a), 5 μm in (b,c), and 50 μm in the inset of (a) and inset of (d).

there is a small redshift of the peak position of the interlayer emission A2 as the temperature increases. This phenomenon has also been observed in other material systems,[54] and it may be associated with the temperature-dependent band gap evolution of both $(4,4\text{-DFPD})_2PbI_4$ and R-NPB, which can lead to the variation of band alignments. Another interesting feature is the variation of the relative intensity between A1 and A2 when the temperature changes, as revealed in Figure 4g. In Figure 4g, we normalize the intensity of A1 at different temperatures to be the same. The intensity ratio of A2 to A1 increases as the temperature increases. For example, the ratio of A2 to A1 is about 0.14 at 120 K, and it increases to about 0.57 at 240 K. The temperature-dependent PL spectra of another R-NPB/$(4,4\text{-DFPD})_2PbI_4$ heterostructure where the R-NPB top layer is very thin have also been collected, and a similar observation can be found (Figure S13). The faster decay of A1 emission with increasing temperature (compared with that of A2) can cause such a variation in their relative intensities.

The exciton dynamics in the R-NPB/$(4,4\text{-DFPD})_2PbI_4$ heterostructure can also be adjusted by changing the excitation fluence. Figure 5a displays the normalized PL spectra (with A2 peaks normalized to be the same) of an R-NPB/$(4,4\text{-DFPD})_2PbI_4$ heterostructure at different excitation fluences recorded at 240 K (see more spectra in Figure S14a). The relative intensity between A1 and A2 changes dramatically as

https://doi.org/10.1021/jacs.2c07069
J. Am. Chem. Soc. 2022, 144, 17588−17596

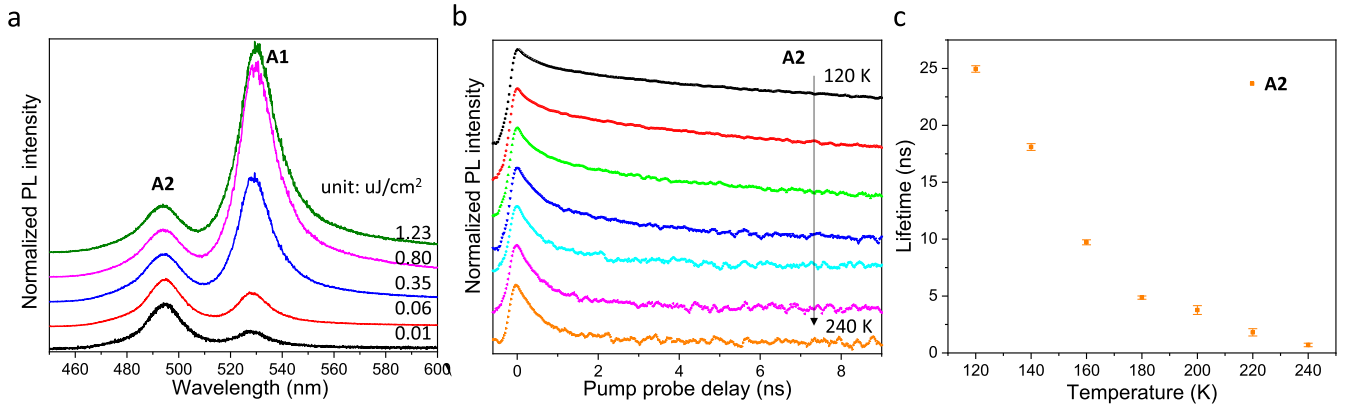

Figure 5. Exciton dynamics in R-NPB/$(4,4\text{-DFPD})_2PbI_4$ heterostructures. (a) Normalized PL spectra of an R-NPB/$(4,4\text{-DFPD})_2PbI_4$ heterostructure at 240 K under different excitation fluences, which show the fluence-dependent emission characteristics of this heterostructure. (b) Temperature-dependent TRPL spectra of an R-NPB/$(4,4\text{-DFPD})_2PbI_4$ heterostructure. The temperature range is from 120 to 240 K with a step increment of 20 K. The signals were collected under an excitation fluence of 0.06 $\mu J/cm^2$. The detection window is at 490 nm for A2 emission. (c) Exciton lifetime for the interlayer A2 emission at different temperatures extracted from curves in (b).

the excitation fluence changes. As we can see, the intensity of A2 is lower than that of A1 when the excitation fluence is above 0.06 $\mu J/cm^2$. However, when the excitation fluence reduces to 0.06 $\mu J/cm^2$ or less, the interlayer A2 emission becomes stronger than A1. Such a signal reversal can also be found in another R-NPB/$(4,4\text{-DFPD})_2PbI_4$ heterostructure as shown in Figure S14b. For the R-NPB/$(4,4\text{-DFPD})_2PbI_4$ heterostructure in Figure S14b, its critical fluence for dominant interlayer A2 emission is less than 0.06 $\mu J/cm^2$ (the intensity of A2 emission becomes higher than that of A1 when the fluence reduces to 0.01 $\mu J/cm^2$ based on the measured data). This fluence-modulated PL intensity switching is believed to be associated with the relative thickness of the $(4,4\text{-DFPD})_2PbI_4$ layer and the R-NPB layer. Since the excitation light penetrates the R-NPB top layer first, the thicker the R-NPB layer, the more photons will be absorbed by it, leading to less excitation in the bottom $(4,4\text{-DFPD})_2PbI_4$ layer relatively. It is noted that the observed interlayer emission behaves differently from some observations on the blueshift of interlayer emission in the conventional transition metal dichalcogenide heterostructure.[56] The relationship between the PL intensity and the fluence for each emission has also been investigated at 240 K (Figure S15). As we can see, there is an almost linear relationship between the fluence and the PL intensity for the A2 emission at low fluences ($\leq$1.54 $\mu J/cm^2$). This suggests that the luminescence could likely originate from purely first-order excitonic emission under low carrier density conditions. However, there is a transition from linear to superlinear when the fluence is over 1.54 $\mu J/cm^2$. It reveals the increased contribution from the free electron/hole bimolecular recombination and suggests that the interlayer excitons tend to dissociate into free charge carriers when the carrier density becomes higher.[57] For the interlayer A1 exciton emission, the integrated PL intensity shows an over linear relationship ($\propto P^{1.4}$) for the whole fluence range. The deviation from a purely excitonic behavior can be associated with competitions from the bimolecular electron/hole recombination process in our $(4,4\text{-DFPD})_2PbI_4$.

Considering the carrier transfer across the interface of a heterostructure, interlayer excitons usually have much longer lifetimes than its intralayer emissions.[52,58,59] To confirm this feature for our designed material system, time-resolved PL (TRPL) measurements on an R-NPB/$(4,4\text{-DFPD})_2PbI_4$ heterostructure are conducted, as shown in Figures 5b and S16a. Figure 5b displays a series of TRPL measurements for interlayer A2 exciton at different temperatures. The exciton lifetime gradually increases as the temperature decreases from 240 to 120 K, which can be attributed to the reduction of phonon scattering.[60,61] The exciton lifetime for interlayer A2 emission extracted from these curves is plotted in Figure 5c. As we can see, it increases to about 25 ns when the temperature reaches 120 K. For the A1 emission, its exciton lifetime has a similar trend as A2 (Figure S16b). It is worth noting that a lifetime of ~25 ns for the interlayer A2 exciton at 120 K is substantial. For instance, the interlayer exciton lifetime is around 1.8 ns at 20 K in the $MoSe_2/WSe_2$ heterostructure.[59] The polarized optical feature of A2 emission has also been studied considering R-NPB is a right-handed chiral 2D perovskite (Figures S17 and S18). The PL intensity is a little bit higher for right circularly polarized light excitation than left circularly polarized light, although the difference is not so obvious, which may be attributed to the extremely small circular dichroism in the wavelength of interest.[6]

CONCLUSIONS

We report a liquid-phase van der Waals epitaxial growth of a 2D RP hybrid perovskite $(4,4\text{-DFPD})_2PbI_4$ on muscovite mica and a design of R-NPB/$(4,4\text{-DFPD})_2PbI_4$ perovskite−perovskite vertical heterostructures with interlayer emission. The $(4,4\text{-DFPD})_2PbI_4$ belts grown on mica can be unit-cell thin and are well aligned, allowing further integration into arbitrary heterostructures with other 2D perovskites and potentially other layered materials such as graphene, hexagonal boron nitride, and transition metal dichalcogenides. The emission intensity of the interlayer exciton A2 increases as the temperature decreases, and its peak position shows a small redshift with the increase of temperature from 120 to 240 K. The relative emission strength between this interlayer exciton and the intralayer exciton A1 can be adjusted by changing the excitation fluences. A carrier recombination lifetime of about 25 ns at 120 K has been identified for this interlayer emission. Our findings suggest an avenue to grow and align 2D halide perovskites in solution and indicate 2D RP perovskite−perovskite heterostructures as a feasible platform to explore exciton physics.

https://doi.org/10.1021/jacs.2c07069
J. Am. Chem. Soc. 2022, 144, 17588−17596

METHODS

Growth of Epitaxial (4,4-DFPD)$_2$PbI$_4$ on Mica. PbI_2, $PbBr_2$, HI solution (47 wt % in water), HBr solution (47 wt % in water), *R*-1-(1-naphthyl)ethylamine, and 4,4-difluoropiperidinium hydrochloride (97%) were purchased from Sigma-Aldrich Corporation. We first synthesized bulk (4,4-DFPD)$_2$PbI$_4$ single crystals based on the method in ref 8. Then, 0.4 mmol bulk (4,4-DFPD)$_2$PbI$_4$ crystals were put in 20 mL of HI solution, and the solution was evaporated under ~50 °C for 3 h to achieve a nearly saturated state. The solution was cooled down to room temperature and kept in a closed glass vial as the growth solution. A piece of muscovite mica was separated into two parts along its cleavage facet. Several microliters of this saturated solution were dispensed onto the fresh and clean surface of the split mica. A flat liquid layer would form on the mica substrate. The mica sheet covered with saturated (4,4-DFPD)$_2$PbI$_4$ solution was then placed in a chemical hood at room temperature for 6−12 h, during which HI and water molecules in the solution evaporated steadily, leading to the nucleation and growth of (4,4-DFPD)$_2$PbI$_4$. (4,4-DFPD)$_2$PbI$_4$ perovskite belts grown on the mica substrate were then obtained and used for other characterizations and tests. For the R-NPB RP perovskite, it was synthesized according to ref 48. Thin R-NPB sheets were then obtained by simply exfoliating the synthesized bulk R-NPB crystals with thermal release tape.

Structural and Microscopy Characterizations. XRD spectra were collected on a Panalytical X'Pert PRO MPD system with a Bruker D8 Discover X-ray diffractometer. The morphology of (4,4-DFPD)$_2$PbI$_4$ belt arrays on mica was characterized by a Nikon Eclipse Ti-S inverted optical microscope. EBSD data were collected in a Carl Zeiss Ultra 1540 EsB SEM-FIB system equipped with a NordlysNano detector from Oxford Instruments. The crystallographic orientation data were collected and analyzed by Aztec software from Oxford Instruments. An Asylum Research MFP-3D atomic force microscope was used to measure the thickness of (4,4-DFPD)$_2$PbI$_4$ belts under contact mode. A cantilever (AC240TM-R3) with a spring constant of 2 N/m and a tip radius of 15 nm was used.

PL Measurements. All PL measurements were conducted on a customized system (a Nikon Eclipse Ti-S inverted optical microscope, a Thorlabs 4 Megapixel Monochrome Scientific CCD camera, and a Princeton Instruments SP-2358 spectrograph). Samples were excited using a PicoQuant 405 nm pulsed diode laser whose power can be adjusted step-by-step. For temperature-dependent PL measurements, an INSTEC HCS302 microscope cryostat was used to support the sample and to provide low-temperature conditions *via* liquid nitrogen pumping.

GSAM Calculation. This method analyzes possible epitaxial relationships based on the overlayer−substrate pairs of superlattices formed at the interface. It pursues a high density of closely coincident lattice sites and a minimal superlattice area mismatch between the epitaxial overlayer and the substrate. In our simulation, we define the unit vectors of the substrate superlattice (mica) as u_1 and v_1 with an angle θ_1 between them and the unit vectors of the overlayer superlattice [(4,4-DFPD)$_2$PbI$_4$] as u_2 and v_2 with an angle θ_2 between them. A_1 and A_2 are the substrate and overlayer superlattice areas, respectively. The rotation angle γ between these two superlattices is defined as the angle between u_1 and u_2. The superlattice area mismatch (ΔA) is defined as $\Delta A = A(\Delta u/u + \Delta v/v + \Delta\theta/\tan\theta)$; for small superlattice mismatches, $A \approx A_1$ (or A_2), $u \approx u_1$ (or u_2), $v \approx v_1$ (or v_2), $\theta \approx \theta_1$ (or θ_2), $\Delta u = |u_1 - u_2|$, $\Delta v = |v_1 - v_2|$, and $\Delta\theta = |\theta_1 - \theta_2|$. The smaller the value of ΔA and the smaller A, the higher the configurational probability. In the simulation, the maximums of A, $\Delta u/u$, $\Delta v/v$, and $\Delta\theta/\theta$ are limited to 200 Å, 10%, 10%, and 10%, respectively.

ASSOCIATED CONTENT

Supporting Information

The Supporting Information is available free of charge at https://pubs.acs.org/doi/10.1021/jacs.2c07069.

Structural characterization of (4,4-DFPD)$_2$PbI$_4$ and R-NPB, PL studies of R-NPB crystal and R-NPB/(4,4-DFPD)$_2$PbI$_4$ heterostructures, and temperature-dependent lifetime study of intralayer exciton in R-NPB/(4,4-DFPD)$_2$PbI$_4$ heterostructures (PDF)

AUTHOR INFORMATION

Corresponding Author

Jian Shi − *Department of Materials Science and Engineering, Rensselaer Polytechnic Institute, Troy, New York 12180, United States;* orcid.org/0000-0003-2115-2225; Email: shij4@rpi.edu

Authors

Lifu Zhang − *Department of Materials Science and Engineering, Rensselaer Polytechnic Institute, Troy, New York 12180, United States*

Jie Jiang − *Department of Materials Science and Engineering, Rensselaer Polytechnic Institute, Troy, New York 12180, United States*

Yang Hu − *Department of Materials Science and Engineering, Rensselaer Polytechnic Institute, Troy, New York 12180, United States*

Zonghuan Lu − *Department of Physics, Applied Physics, and Astronomy, Rensselaer Polytechnic Institute, Troy, New York 12180, United States;* orcid.org/0000-0003-2375-8247

Xixing Wen − *Department of Physics, Applied Physics, and Astronomy, Rensselaer Polytechnic Institute, Troy, New York 12180, United States*

Saloni Pendse − *Department of Materials Science and Engineering, Rensselaer Polytechnic Institute, Troy, New York 12180, United States*

Ru Jia − *Department of Materials Science and Engineering, Rensselaer Polytechnic Institute, Troy, New York 12180, United States*

Gwo-Ching Wang − *Department of Physics, Applied Physics, and Astronomy, Rensselaer Polytechnic Institute, Troy, New York 12180, United States*

Toh-Ming Lu − *Department of Physics, Applied Physics, and Astronomy, Rensselaer Polytechnic Institute, Troy, New York 12180, United States*

Complete contact information is available at: https://pubs.acs.org/10.1021/jacs.2c07069

Notes

The authors declare no competing financial interest.

Data availability: Data are available upon reasonable requests from the corresponding authors.

Code availability: Codes are available upon reasonable requests from the corresponding authors.

ACKNOWLEDGMENTS

J.S., T.-M.L., and G.-C.W. acknowledge the New York State's Empire State Development's Division of Science, Technology and Innovation through Focus Center Contract C180117. J.S. acknowledges support from the US National Science Foundation under award numbers 2024972 and 2031692.

REFERENCES

(1) Shi, E.; Gao, Y.; Finkenauer, B. P.; Coffey, A. H.; Dou, L. Two-dimensional halide perovskite nanomaterials and heterostructures. *Chem. Soc. Rev.* **2018**, *47*, 6046−6072.

(2) Blancon, J.-C.; Even, J.; Stoumpos, C.; Kanatzidis, M.; Mohite, A. D. Semiconductor physics of organic−inorganic 2D halide perovskites. *Nat. Nanotechnol.* **2020**, *15*, 969−985.
(3) Pan, D.; Fu, Y.; Spitha, N.; Zhao, Y.; Roy, C. R.; Morrow, D. J.; Kohler, D. D.; Wright, J. C.; Jin, S. Deterministic fabrication of arbitrary vertical heterostructures of two-dimensional Ruddlesden−Popper halide perovskites. *Nat. Nanotechnol.* **2021**, *16*, 159−165.
(4) Wygant, B. R.; Ye, A. Z.; Dolocan, A.; Vu, Q.; Abbot, D. M.; Mullins, C. B. Probing the degradation chemistry and enhanced stability of 2D organolead halide perovskites. *J. Am. Chem. Soc.* **2019**, *141*, 18170−18181.
(5) Na Quan, L.; Ma, D.; Zhao, Y.; Voznyy, O.; Yuan, H.; Bladt, E.; Pan, J.; García de Arquer, F. P.; Sabatini, R.; Piontkowski, Z. Edge stabilization in reduced-dimensional perovskites. *Nat. Commun.* **2020**, *11*, 170.
(6) Jana, M. K.; Song, R.; Liu, H.; Khanal, D. R.; Janke, S. M.; Zhao, R.; Liu, C.; Valy Vardeny, Z.; Blum, V.; Mitzi, D. B. Organic-to-inorganic structural chirality transfer in a 2D hybrid perovskite and impact on Rashba-Dresselhaus spin-orbit coupling. *Nat. Commun.* **2020**, *11*, 4699.
(7) Lu, H.; Wang, J.; Xiao, C.; Pan, X.; Chen, X.; Brunecky, R.; Berry, J. J.; Zhu, K.; Beard, M. C.; Vardeny, Z. V. Spin-dependent charge transport through 2D chiral hybrid lead-iodide perovskites. *Sci. Adv.* **2019**, *5*, No. eaay0571.
(8) Zhang, H.-Y.; Song, X.-J.; Chen, X.-G.; Zhang, Z.-X.; You, Y.-M.; Tang, Y.-Y.; Xiong, R.-G. Observation of vortex domains in a two-dimensional lead iodide perovskite ferroelectric. *J. Am. Chem. Soc.* **2020**, *142*, 4925−4931.
(9) Chen, X.-G.; Song, X.-J.; Zhang, Z.-X.; Zhang, H.-Y.; Pan, Q.; Yao, J.; You, Y.-M.; Xiong, R.-G. Confinement-driven ferroelectricity in a two-dimensional hybrid lead iodide perovskite. *J. Am. Chem. Soc.* **2020**, *142*, 10212−10218.
(10) Chen, Z.; Guo, Y.; Wertz, E.; Shi, J. Merits and Challenges of Ruddlesden−Popper Soft Halide Perovskites in Electro-Optics and Optoelectronics. *Adv. Mater.* **2019**, *31*, 1803514.
(11) Straus, D. B.; Kagan, C. R. Electrons, excitons, and phonons in two-dimensional hybrid perovskites: connecting structural, optical, and electronic properties. *J. Phys. Chem. Lett.* **2018**, *9*, 1434−1447.
(12) Quan, L. N.; Zhao, Y.; García de Arquer, F. P.; Sabatini, R.; Walters, G.; Voznyy, O.; Comin, R.; Li, Y.; Fan, J. Z.; Tan, H. Tailoring the energy landscape in quasi-2D halide perovskites enables efficient green-light emission. *Nano Lett.* **2017**, *17*, 3701−3709.
(13) Mao, L.; Stoumpos, C. C.; Kanatzidis, M. G. Two-dimensional hybrid halide perovskites: principles and promises. *J. Am. Chem. Soc.* **2018**, *141*, 1171−1190.
(14) Fu, Y.; Zhu, H.; Chen, J.; Hautzinger, M. P.; Zhu, X.-Y.; Jin, S. Metal halide perovskite nanostructures for optoelectronic applications and the study of physical properties. *Nat. Rev. Mater.* **2019**, *4*, 169−188.
(15) Ortiz-Cervantes, C.; Carmona-Monroy, P.; Solis-Ibarra, D. Two-dimensional halide perovskites in solar cells: 2D or not 2D? *ChemSusChem* **2019**, *12*, 1560−1575.
(16) Tanaka, K.; Kondo, T. Bandgap and exciton binding energies in lead-iodide-based natural quantum-well crystals. *Sci. Technol. Adv. Mater.* **2003**, *4*, 599−604.
(17) Even, J.; Pedesseau, L.; Katan, C. Understanding quantum confinement of charge carriers in layered 2D hybrid perovskites. *Chemphyschem* **2014**, *15*, 3733−3741.
(18) Katan, C.; Mercier, N.; Even, J. Quantum and dielectric confinement effects in lower-dimensional hybrid perovskite semiconductors. *Chem. Rev.* **2019**, *119*, 3140−3192.
(19) Blancon, J.-C.; Stier, A. V.; Tsai, H.; Nie, W.; Stoumpos, C. C.; Traoré, B.; Pedesseau, L.; Kepenekian, M.; Katsutani, F.; Noe, G. Scaling law for excitons in 2D perovskite quantum wells. *Nat. Commun.* **2018**, *9*, 2254.
(20) Geim, A. K.; Grigorieva, I. V. Van der Waals heterostructures. *Nature* **2013**, *499*, 419−425.
(21) Novoselov, K.; Mishchenko, o. A.; Carvalho, o. A.; Castro Neto, A. C. 2D materials and van der Waals heterostructures. *Science* **2016**, *353*, aac9439.
(22) Özçelik, V. O.; Azadani, J. G.; Yang, C.; Koester, S. J.; Low, T. Band alignment of two-dimensional semiconductors for designing heterostructures with momentum space matching. *Phys. Rev. B* **2016**, *94*, 035125.
(23) Jin, C.; Ma, E. Y.; Karni, O.; Regan, E. C.; Wang, F.; Heinz, T. F. Ultrafast dynamics in van der Waals heterostructures. *Nat. Nanotechnol.* **2018**, *13*, 994−1003.
(24) Rivera, P.; Yu, H.; Seyler, K. L.; Wilson, N. P.; Yao, W.; Xu, X. Interlayer valley excitons in heterobilayers of transition metal dichalcogenides. *Nat. Nanotechnol.* **2018**, *13*, 1004−1015.
(25) Mak, K. F.; Shan, J. Opportunities and challenges of interlayer exciton control and manipulation. *Nat. Nanotechnol.* **2018**, *13*, 974−976.
(26) Wang, N.; Cheng, L.; Ge, R.; Zhang, S.; Miao, Y.; Zou, W.; Yi, C.; Sun, Y.; Cao, Y.; Yang, R. Perovskite light-emitting diodes based on solution-processed self-organized multiple quantum wells. *Nat. Photonics* **2016**, *10*, 699−704.
(27) Proppe, A. H.; Quintero-Bermudez, R.; Tan, H.; Voznyy, O.; Kelley, S. O.; Sargent, E. H. Synthetic control over quantum well width distribution and carrier migration in low-dimensional perovskite photovoltaics. *J. Am. Chem. Soc.* **2018**, *140*, 2890−2896.
(28) Wang, J.; Li, J.; Tan, Q.; Li, L.; Zhang, J.; Zang, J.; Tan, P.; Zhang, J.; Li, D. Controllable synthesis of two-dimensional Ruddlesden−Popper-type perovskite heterostructures. *J. Phys. Chem. Lett.* **2017**, *8*, 6211−6219.
(29) Fu, Y.; Zheng, W.; Wang, X.; Hautzinger, M. P.; Pan, D.; Dang, L.; Wright, J. C.; Pan, A.; Jin, S. Multicolor heterostructures of two-dimensional layered halide perovskites that show interlayer energy transfer. *J. Am. Chem. Soc.* **2018**, *140*, 15675−15683.
(30) Wang, J.; Li, J.; Lan, S.; Fang, C.; Shen, H.; Xiong, Q.; Li, D. Controllable growth of centimeter-sized 2D perovskite heterostructures for highly narrow dual-band photodetectors. *ACS Nano* **2019**, *13*, 5473−5484.
(31) Kuo, M.-Y.; Spitha, N.; Hautzinger, M. P.; Hsieh, P.-L.; Li, J.; Pan, D.; Zhao, Y.; Chen, L.-J.; Huang, M. H.; Jin, S. Distinct Carrier Transport Properties Across Horizontally vs Vertically Oriented Heterostructures of 2D/3D Perovskites. *J. Am. Chem. Soc.* **2021**, *143*, 4969−4978.
(32) Radoslovich, E. The structure of muscovite, $KAl_2(Si_3Al)O_{10}(OH)_2$. *Acta Crystallogr.* **1960**, *13*, 919−932.
(33) Sun, X.; Lu, Z.; Xie, W.; Wang, Y.; Shi, J.; Zhang, S.; Washington, M. A.; Lu, T.-M. van der Waals epitaxy of CdS thin films on single-crystalline graphene. *Appl. Phys. Lett.* **2017**, *110*, 153104.
(34) Chen, Z.; Wang, Y.; Sun, X.; Xiang, Y.; Hu, Y.; Jiang, J.; Feng, J.; Sun, Y.-Y.; Wang, X.; Wang, G.-C. Remote phononic effects in epitaxial ruddlesden−popper halide perovskites. *J. Phys. Chem. Lett.* **2018**, *9*, 6676−6682.
(35) Wen, X.; Lu, Z.; Valdman, L.; Wang, G.-C.; Washington, M.; Lu, T.-M. High-crystallinity epitaxial Sb_2Se_3 thin films on mica for flexible near-infrared photodetectors. *ACS Appl. Mater. Interfaces* **2020**, *12*, 35222−35231.
(36) Xiang, Y.; Xie, S.; Lu, Z.; Wen, X.; Shi, J.; Washington, M.; Wang, G.-C.; Lu, T.-M. Domain boundaries in incommensurate epitaxial layers on weakly interacting substrates. *J. Appl. Phys.* **2021**, *130*, 065301.
(37) Wright, A. D.; Verdi, C.; Milot, R. L.; Eperon, G. E.; Pérez-Osorio, M. A.; Snaith, H. J.; Giustino, F.; Johnston, M. B.; Herz, L. M. Electron−phonon coupling in hybrid lead halide perovskites. *Nat. Commun.* **2016**, *7*, 11755.
(38) Dar, M. I.; Jacopin, G.; Meloni, S.; Mattoni, A.; Arora, N.; Boziki, A.; Zakeeruddin, S. M.; Rothlisberger, U.; Grätzel, M. Origin of unusual bandgap shift and dual emission in organic-inorganic lead halide perovskites. *Sci. Adv.* **2016**, *2*, No. e1601156.
(39) Frost, J. M.; Butler, K. T.; Brivio, F.; Hendon, C. H.; van Schilfgaarde, M.; Walsh, A. Atomistic origins of high-performance in hybrid halide perovskite solar cells. *Nano Lett.* **2014**, *14*, 2584−2590.

https://doi.org/10.1021/jacs.2c07069
J. Am. Chem. Soc. 2022, 144, 17588−17596

(40) Wang, S.; Huang, M.; Wu, Y. N.; Chen, S. Absolute Volume Deformation Potentials of Inorganic ABX3 Halide Perovskites: The Chemical Trends. *Adv. Theory Simul.* **2021**, *4*, 2100060.
(41) Dou, L.; Wong, A. B.; Yu, Y.; Lai, M.; Kornienko, N.; Eaton, S. W.; Fu, A.; Bischak, C. G.; Ma, J.; Ding, T. Atomically thin two-dimensional organic-inorganic hybrid perovskites. *Science* **2015**, *349*, 1518−1521.
(42) Liu, J.; Xue, Y.; Wang, Z.; Xu, Z.-Q.; Zheng, C.; Weber, B.; Song, J.; Wang, Y.; Lu, Y.; Zhang, Y. Two-dimensional $CH_3NH_3PbI_3$ perovskite: synthesis and optoelectronic application. *ACS Nano* **2016**, *10*, 3536−3542.
(43) Li, D.; Wang, G.; Cheng, H.-C.; Chen, C.-Y.; Wu, H.; Liu, Y.; Huang, Y.; Duan, X. Size-dependent phase transition in methylammonium lead iodide perovskite microplate crystals. *Nat. Commun.* **2016**, *7*, 11330.
(44) Oksenberg, E.; Sanders, E.; Popovitz-Biro, R.; Houben, L.; Joselevich, E. Surface-guided $CsPbBr_3$ perovskite nanowires on flat and faceted sapphire with size-dependent photoluminescence and fast photoconductive response. *Nano Lett.* **2018**, *18*, 424−433.
(45) Wang, Y.; Gao, L.; Yang, Y.; Xiang, Y.; Chen, Z.; Dong, Y.; Zhou, H.; Cai, Z.; Wang, G.-C.; Shi, J. Nontrivial strength of van der Waals epitaxial interaction in soft perovskites. *Phys. Rev. Mater.* **2018**, *2*, 076002.
(46) Parrott, E. S.; Patel, J. B.; Haghighirad, A.-A.; Snaith, H. J.; Johnston, M. B.; Herz, L. M. Growth modes and quantum confinement in ultrathin vapour-deposited $MAPbI_3$ films. *Nanoscale* **2019**, *11*, 14276−14284.
(47) Liu, Z.; Li, Y.; Guan, X.; Mi, Y.; Al-Hussain, A.; Ha, S. T.; Chiu, M.-H.; Ma, C.; Amer, M. R.; Li, L.-J. One-step vapor-phase synthesis and quantum-confined exciton in single-crystal platelets of hybrid halide perovskites. *J. Phys. Chem. Lett.* **2019**, *10*, 2363−2371.
(48) Jana, M. K.; Song, R.; Liu, H.; Khanal, D. R.; Janke, S. M.; Zhao, R.; Liu, C.; Valy Vardeny, Z. V.; Blum, V.; Mitzi, D. B. Organic-to-inorganic structural chirality transfer in a 2D hybrid perovskite and impact on Rashba-Dresselhaus spin-orbit coupling. *Nat. Commun.* **2020**, *11*, 4699.
(49) Butler, K. T.; Frost, J. M.; Walsh, A. Band alignment of the hybrid halide perovskites $CH_3NH_3PbCl_3$, $CH_3NH_3PbBr_3$ and $CH_3NH_3PbI_3$. *Mater. Horiz.* **2015**, *2*, 228−231.
(50) Finkman, E.; Sturge, M.; Tamargo, M. X-point excitons in AlAs/GaAs superlattices. *Appl. Phys. Lett.* **1986**, *49*, 1299−1301.
(51) Finkman, E.; Planel, R. Photoluminescence nonlinearities in mixed type I−type II quantum well heterostructures. *Appl. Phys. Lett.* **1998**, *72*, 2604−2606.
(52) Danan, G.; Etienne, B.; Mollot, F.; Planel, R.; Jean-Louis, A.; Alexandre, F.; Jusserand, B.; Le Roux, G.; Marzin, J.; Savary, H. Optical evidence of the direct-to-indirect-gap transition in GaAs-AlAs short-period superlattices. *Phys. Rev. B: Condens. Matter Mater. Phys.* **1987**, *35*, 6207.
(53) Karni, O.; Barré, E.; Lau, S. C.; Gillen, R.; Ma, E. Y.; Kim, B.; Watanabe, K.; Taniguchi, T.; Maultzsch, J.; Barmak, K. Infrared interlayer exciton emission in MoS_2/WSe_2 heterostructures. *Phys. Rev. Lett.* **2019**, *123*, 247402.
(54) Chen, Y.; Liu, Z.; Li, J.; Cheng, X.; Ma, J.; Wang, H.; Li, D. Robust interlayer coupling in two-dimensional perovskite/monolayer transition metal dichalcogenide heterostructures. *ACS Nano* **2020**, *14*, 10258−10264.
(55) Pendse, S.; Jiang, J.; Guo, Y.; Zhang, L.; Chen, Z.; Lu, Z.; Wang, Y.; Hu, Y.; Li, S.; Feng, J. Unit-Cell-Thick Oxide Synthesis by Film-Based Scavenging. *J. Phys. Chem. C* **2020**, *124*, 8394−8400.
(56) Liu, E.; Barré, E.; van Baren, J.; Wilson, M.; Taniguchi, T.; Watanabe, K.; Cui, Y.-T.; Gabor, N. M.; Heinz, T. F.; Chang, Y.-C. Signatures of moiré trions in WSe2/MoSe2 heterobilayers. *Nature* **2021**, *594*, 46−50.
(57) Xing, G.; Wu, B.; Wu, X.; Li, M.; Du, B.; Wei, Q.; Guo, J.; Yeow, E. K.; Sum, T. C.; Huang, W. Transcending the slow bimolecular recombination in lead-halide perovskites for electroluminescence. *Nat. Commun.* **2017**, *8*, 14558.
(58) Dawson, P.; Moore, K.; Foxon, C.; 't Hooft, G.; van Hal, R. Photoluminescence decay time studies of type II GaAs/AlAs quantum-well structures. *J. Appl. Phys.* **1989**, *65*, 3606−3609.
(59) Rivera, P.; Schaibley, J. R.; Jones, A. M.; Ross, J. S.; Wu, S.; Aivazian, G.; Klement, P.; Seyler, K.; Clark, G.; Ghimire, N. J. Observation of long-lived interlayer excitons in monolayer $MoSe_2$−WSe_2 heterostructures. *Nat. Commun.* **2015**, *6*, 6242.
(60) Guo, Z.; Wu, X.; Zhu, T.; Zhu, X.; Huang, L. Electron−phonon scattering in atomically thin 2D perovskites. *ACS Nano* **2016**, *10*, 9992−9998.
(61) Chen, T.; Chen, W.-L.; Foley, B. J.; Lee, J.; Ruff, J. P.; Ko, J. P.; Brown, C. M.; Harriger, L. W.; Zhang, D.; Park, C. Origin of long lifetime of band-edge charge carriers in organic−inorganic lead iodide perovskites. *Proc. Natl. Acad. Sci. U.S.A.* **2017**, *114*, 7519−7524.

https://doi.org/10.1021/jacs.2c07069
J. Am. Chem. Soc. 2022, 144, 17588−17596